TUDelft

Delft University of Technology

Robust additive manufacturable Ni superalloys designed by the integrated optimization of local elemental segregation and cracking susceptibility criteria

Yu, Hao; Fu, Jiabo; Wang, Chenchong; Chen, Yinping; Wang, Lingyu; Fang, Haixing; Li, Jinguo; van der Zwaag, Sybrand; Xu, Wei

Important note
To cite this publication, please use the final published version (if applicable).
Please check the document version above.

Robust additive manufacturable Ni superalloys designed by the integrated optimization of local elemental segregation and cracking susceptibility criteria

Hao Yu [a], Jiabo Fu [a], Chenchong Wang [a], Yinping Chen [a], Lingyu Wang [a], Haixing Fang [b,c,d], Jinguo Li [e], Sybrand van der Zwaag [f], Wei Xu [a,*]

[a] *State Key Laboratory of Rolling and Automation, Northeastern University, Shenyang 110819, China*
[b] *European Synchrotron Radiation Facility, 71 Avenue des Martyrs, Grenoble 380000, France*
[c] *Université Grenoble Alpes, Grenoble INP, CNRS SIMaP, 1130 Rue de la Piscine, Saint Martin d'Hères 38402, France*
[d] *Université de Lyon, INSA Lyon, CNRS MATEIS, Villeurbanne 69621, France*
[e] *Institute of Metal Research, Chinese Academy of Sciences, Shenyang 110016, China*
[f] *Novel Aerospace Materials Group, Faculty of Aerospace Engineering, Delft University of Technology, 2629 HS, Delft, the Netherlands*

ARTICLE INFO

ABSTRACT

To achieve an effective design of additively manufacturable Ni superalloys with decent service performance, a hybrid computational design model has been developed, where the strategy to tailor local elemental segregations was integrated within a scheme of minimizing the cracking susceptibility. More specifically, the phase boundary of primary NbC / γ matrix was introduced into the design routine to tune the spatial distribution of critical solutes at an atomic scale, thereby inhibiting the formation of borides and segregation-induced cracking. Based on the output of the design, new grades of Ni superalloy have been developed with excellent additive manufacturability, as confirmed by the robustness of printing parameters in fabricating low-defect-density samples. The capability of the phase boundaries to evenly distribute boron atoms was validated experimentally, and the cracking induced by uncontrolled boron segregation at grain boundaries was effectively prevented. The newly designed alloys showed good tensile properties and decent oxidation resistance at different service temperatures, which are comparable to those of conventionally produced superalloys. The finding that phase boundaries can be employed to prevent undesirable clustering of boron atoms can be extended to manipulate the distributions of other critical elements, which provides a new path for designing novel Ni superalloys with balanced printability and mechanical properties.

1. Introduction

Ni superalloys for aviation and space applications present an interesting potential for additive manufacturing (AM) as the components to be produced with these advanced high temperature alloys have increasingly complex geometries and dimensions which are inefficiently to be fabricated through conventional manufacturing methods [1–3]. By now, it remains challenging to produce high-density components for most of the existing Ni commercial superalloys, because the high cooling rates and the spatially variable temperature gradients during additive manufacturing generally lead to severe cracking [4–6]. To solve this problem, researchers have made extensive efforts to study and optimize the AM processing parameters, including scanning strategy, beam power

and energy inputs [7–11]. However, it has been progressively realized that the current existing commercial Ni superalloys, most of which have been designed and optimized for conventional manufacturing methods, may not fit the distinctly different metallurgical conditions of AM. Hence, new alloy compositions tailored to match the AM conditions need to be developed [12–18].

Two main strategies have been proposed to design and optimize the chemical compositions to obtain additive manufacturable Ni superalloys. The first strategy focuses on avoiding AM induced cracks, in particular hot cracks forming in the near-solidification state and strain-age cracks forming in the fully solidified state [14,17,19]. A few cracking susceptibility criteria have been proposed to classify the likelihood of crack formation. For the hot cracks, the proposed crack

---

* Corresponding author.
   E-mail address: xuwei@ral.neu.edu.cn (W. Xu).

susceptibility criteria, such as the critical solidification temperature range theory [20], the Rappaz-Drezet-Gremaud criterion [21] and the hot crack susceptibility index [22], are linked to the solidification features during AM processing. In contrast, the susceptibility to the strain-age cracking (SAC) is defined according to the stress induced by the precipitation of the γ' phase from the solid solution which compromises local ductility. These susceptibility metrics include an empirical index that describes the tendency of γ' precipitates formation [14] and a criterion that quantifies the kinetics of γ' precipitate formation [17]. Based on the susceptibility of hot cracking and strain-age cracking, novel compositions for additive manufacturable Ni superalloys can be screened computationally over a wide range of potential compositions to avoid the cracking issue during AM processing. However, the highly uneven spatial variation of elemental distribution, ranging from the macro-scale down to near atomic scale, as a result of the rapid solidification and the successive repeated thermal cycles, has not been taken into account in these design parameters yet. Calculations of the crack susceptibility based on bulk average compositions may lead to relevant discrepancies between the predicted and observed cracking tendency [23,24].

An alternative strategy has been proposed taking into account the observation that high cracking susceptibility can originate from the differences in the solidification character as well as the resulting mechanical properties between the dendritic and interdendritic regions [15,16,18]. Therefore, solutes that have a strong segregation tendency upon cooling (both during solidification and the subsequent solid-state stage) are becoming critical. This has led to a number of studies focusing on the influence of elemental partitioning, and selective segregation to minimize the spatial variations of composition-induced features [23,25-27]. Among all critical segregation prone elements, boron has drawn a lot of attention, whilst it can have both positive and negative effects. It is reported that minor boron addition can strongly promote AM cracking, since the uncontrolled boron segregation at grain boundaries will inevitably lead to the formation of low melting borides, which could easily turn into a liquid film at the nearly solidified state or during a reheating stage, and thereby initiate cracking [5,26,28]. However, to simply exclude boron alloying to avoid such cracking is not practical, as B is an efficient strengthening element in improving high-temperature creep-resistance properties for Ni superalloys [29–32]. Hence, attempts have been made to tailor B partitioning behavior by adjusting the concentration of B as well as co-alloying with elements such as Si and C which co-segregate with B at a near atomic scale [16,27]. However, it remains unclear whether such a near-atomic-scale co-segregation can also be triggered over wider composition domain. More recently, the grain refinement method was adopted to tailor the boron distribution [5,33]. In this method, the increased grain boundary area generated by the smaller grains provides a larger interfacial area to trap B atoms, and to avoid the excessive B segregation leading to the formation of low melting phases. Despite the difficulty to achieve grain refinement for Ni superalloys during AM processing, the amount of segregation-induced cracking has been significantly reduced employing this approach.

Today, it is still challenging to obtain an effective design of novel Ni superalloys with robust additive manufacturability. The key to improving the design efficiency and accuracy is to develop a comprehensive model, which means that both the minimization of the crack susceptibility and the suppression of the local element segregation should be considered in a combined manner. Based on the aforementioned studies, introducing high energy boundaries to control boron segregation is expected to be effective. In addition to grain boundaries, phase boundaries being another form of a high energy boundary, may be used to tune the boron distribution. Candidates are the commonly present phase boundaries in Ni superalloys (such as MC carbide / γ, $M_{23}C_6$ carbide / γ interfaces, etc.). To maximize the boron trapping before conditions lead to the formation of borides, the target phases should precipitate primarily in melt during AM processing. This high melting

point criterion largely rules out $M_{23}C_6$ carbides. However, it is reported in literature that boron segregation was observed at MC carbides / γ matrix interfaces [16], and there was a preference of forming boron precursor in the vicinity of primary MC [34,35]. Therefore, it is postulated that the phase boundaries of MC/ γ matrix can be employed to address the boron segregation issue. By controlling the MC carbide to form primary phase boundaries, boron atoms are expected to distribute at the MC / matrix interface, rather than clustering to form borides and initiating cracks at the nearly solidified states. Experimental investigations indeed showed that the presence of specific MC carbides may be relevant to the risk of liquation cracking [36–38]. There is thus a need to select a proper type of MC carbides for manipulating B distribution, which will be discussed in the next section.

In this work, a hybrid alloy design strategy is proposed to achieve an effective design of robust additive manufacturable Ni superalloys. An efficient average composition screening is integrated with a scheme of tuning local elemental segregation. Based on the design output, novel grades of Ni superalloys have been developed, and they show excellent additive manufacturability, with a large processing window to obtain low-defect-density samples. Controlling boron distribution at the phase boundaries of MC carbide and γ matrix has been demonstrated, as confirmed by both first-principle calculations and experimental characterization, while the formation of boron-segregation induced cracking is effectively inhibited. The mechanical properties of the new alloys were found to be comparable to or better than existing conventional superalloys. It is suggested that this new approach to solve the problem related to elemental segregation during the AM processing has a great potential to advance the performance of novel printable Ni superalloys.

2. Alloy design model

2.1. Interface properties of γ / MC phase boundaries

To preliminarily explore the feasibility of employing γ / MC phase boundaries to capture boron atoms, the segregation behaviors of B atoms at the γ / MC interface are simulated using first-principle calculations. Fig. 1(a) shows the supercell structure of a coherent Ni / MC interface with a low energy (001) orientation, which was modeled using an 84-atom interface slab (a Ni slab with 7 layers and an MC slab with 7 layers). The generalized gradient approximation (GGA) with Perdew Burke-Ernzerhof (PBE) was used to evaluate exchange-correlation functionals of the target phase boundaries [39]. The interaction between ionic core and valence electrons were described by plane-wave ultra-soft pseudopotential method. Based on the convergence test, k-point meshes of $4 \times 4 \times 1$ and a plane-wave cutoff energy of 400 eV were applied in the interfacial calculations to ensure an energy convergence of 1×10^{-5} eV/ atom. A vacuum spacing of 10 Å is added along the [001] direction to eliminate the interactions between the interfaces in neighboring supercells across the periodic boundary condition. In Fig 1(a), the possible doping sites for boron atom are labelled, with substitutional and interstitial sites marked by orange and green dots, respectively. The calculations were performed for three types of MC carbides (*M*=Nb, Ti and Ta), which all three form at temperatures where the Ni matrix is in the liquid state.

For configuration shown in Fig 1(a), the segregation energy was calculated as the total energy difference between the Ni / MC supercell with the boron atom occupying the most-stable site in bulk (i.e. the interstitial octahedral site, position 6 in Fig 1a) and that with the boron atom situated at the interface (both substitutional and interstitial sites are considered, position 1–5 in Fig 1a). The segregation energy ($E_{seg\text{-}B}$) is given by [40–42]

$$E_{seg-B} = E_m^{inter} - E_{bulk}^{inter} + \mu_{Hm} \tag{1}$$

where E_m^{inter} denotes the total energy of the Ni / MC supercell with a B atom located at the interface with subscript m denoting the site position,
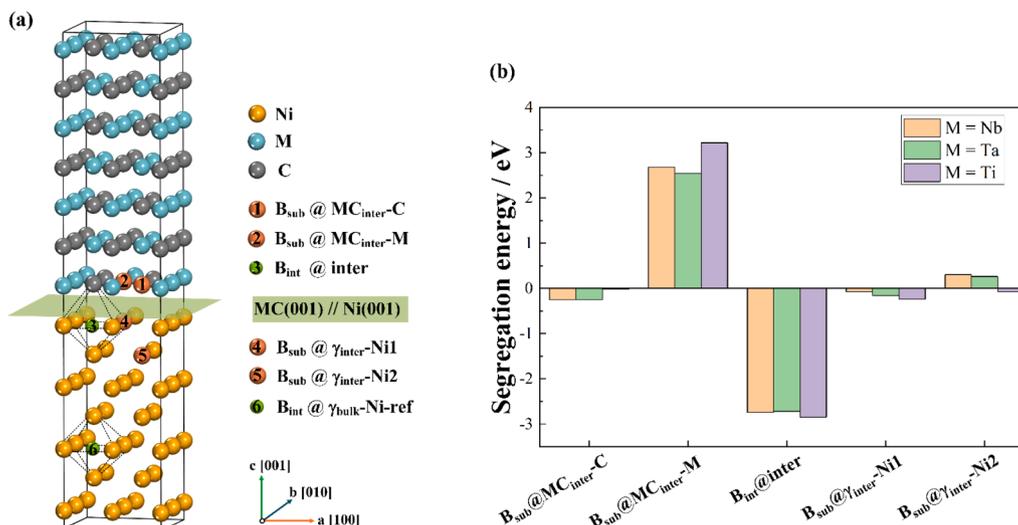
Fig. 1. (a) The supercell structure of γ-Ni / MC (*M*=Nb, Ta and Ti) interface along the (001) plane; (b) segregation energies for interstitial boron at different positions near interface.

and E_{bulk}^{inter} indicates the total energy of the supercell with an interstitial B atom in Ni bulk (i.e., located far from the interface and taken as the reference state), respectively. μ_{Hm} is the atomic energy of the substituted host atom (Hm= Ni, M, C). When the boron atom presents on the interstitial site near the interface, the μ_{Hm} term in Eq. (1) is null. When the boron atom substitutes a C/M/Ni atom, the supercell contains one atom less compared to the reference state, and μ_{Hm} is used to balance the number of atoms of each species. The calculated segregation energies of boron atoms at the (001) Ni/(001) MC interface are presented in Fig. 1 (b). The configurations with a negative segregation energy indicate sites where boron segregation is thermodynamically favored, while the ones with a positive segregation energy value corresponds to unfavorable and unlikely occupations. In particular, the segregation energies for boron atoms at the interstitial sites of γ/MC phase interface can reach values down to around −2.6 eV, indicating a great preference of boron atoms to get enriched interstitially at the target interface.

In general, first-principle calculations are performed for conditions at 0 K as these calculations are more accurate. However, given that boron segregation takes place predominantly at the last stage of solidification during the AM processing [26,33], the segregation energy of elements at γ/MC interface were calculated at solidus temperature as well using molecular dynamics calculation, as presented in Fig. S1 in Supplementary Materials. The results show that at elevated temperature, it is energetically preferable for B atoms to reside at the interstitial sites of γ/MC phase boundaries. Therefore, potential capability of the γ / MC high-energy interfaces to capture boron atoms has been verified by the results of ab initio calculations, and further experimental validations will follow in the next sections.

2.2. Principle of the design model based on overall composition

The framework of hybrid computational design model consists of 4 steps:1) Generate the candidates with different chemical compositions; 2) Screen the compositions by the constraint criteria based on service performances; 3) Determine and rank crack susceptibility of potential compositions meeting the constraints using two quantitative criteria;

The above steps are repeated for at least 10^7 potential compositions. 4) This automatic procedure is followed by an operator assisted procedure to split the potentially optimal solutions into those without MC carbides and those with B-trapping MC primary precipitates.

Firstly, candidates with different compositions were randomly generated by genetic algorithm within the allowed search range for each alloying element, as listed in Table 1. The defined search ranges cover the most densely populated distribution intervals of alloying element concentrations for commercial Ni superalloys, as shown in Fig. S2 in Supplementary Materials. 10 alloying elements have been considered in this work, and their concentrations were uniformly sampled by 32 levels between the predefined minimum and maximum values, yielding potentially 32^{10} candidates. Considering the balance to explore significant amount of solution space and taking into account computational costs, the generation of new solutions was stopped after 10^7 potential compositions been explored.

Secondly, four constraint criteria were imposed to filter potential candidate solutions, so that the performance of potential solutions at service temperature can be assured above the minimum levels. In this work, the service temperature was preset as 900 °C, where the properties including microstructural stability, oxidation resistance and mechanical strengthening effects were taken into consideration. For the microstructural stability, two constraint criteria are imposed: (a) the amount of γ' phase should be higher than 40 % to ensure the proper precipitation strengthening contributions, and (b) the volume fraction of undesirable phase (except γ matrix and γ' precipitates) should be less than 4 % to keep the microstructure stability. The two constrain criteria were defined based on the results of thermodynamic calculation for a wide range of existing Ni commercial alloys. Regarding the oxidation resistance, the merit of oxidation resistance $M_{Oxidation}$ was calculated as a combined consideration of the Gibbs free energy and the effective valence of Al_2O_3, referring to the investigations [43,44], where the corresponding criterion is defined: (c) the value of $M_{Oxidation}$ should be positive to form a continuous alumina scale to guarantee the decent oxidation resistance. Moreover, the effects of solid solution strengthening for the candidate compositions are obtained following the

Table 1
Search ranges (in wt.%) for chemical elements.

	Al	Co	Cr	Mo	Ta	Ti	W	C	B	Nb	Ni
Min.	2	8	5	0	0	0	0	0	0	0	Bal.
Max.	8	15	15	5	10	5	10	0.25	0.25	5	

approaches from [45]. It is thus imposed that (d) the solid solution strengthening effect should be higher than 400 MPa. All thermodynamic features were obtained from the equilibrium calculations at the pre-defined service temperature 900 °C. The detailed descriptions of the above four constraints criteria, and the corresponding physical metallurgy models are described in the Supplementary Material.

Thirdly, each composition meeting all constraint criteria was evaluated and ranked according two criteria for hot cracking: the likelihood of cracking during freezing from the molten state, and the likelihood of strain-age cracking due to stresses building up during microstructure evolution in the solid state. The Freezing Range (FR) is employed as a simple indicator of the hot cracking proneness [14], which is obtained by the Scheil-Gulliver simulation of non-equilibrium solidification.

$$FR = T_{Liquidus}^{SG} - T_{Solidus}^{SG} \tag{2}$$

where $T_{Liquidus}^{SG}$ and $T_{Solidus}^{SG}$ stands for the liquidus and solidus temperature of Scheil-Gulliver solidifications, respectively, and $T_{Solidus}^{SG}$ is obtained by setting the terminal solid fraction 99 %. The boron and carbon atoms were set as fast diffusers to take the back diffusion effects into consideration [46]. A reduced value of FR indicates an improved resistance to hot cracking.

In addition, the precipitation-behavior based criterion to evaluate the strain-ageing crack susceptibility (named as SAC factor) was applied using the evaluation parameter introduced in very recent work by Yu et al. [17], where the SAC factor was defined as the derivative of the γ volume as a function of temperature:

$$SAC = dV_f^\gamma \big/ dT, T \in \left[T_\gamma^*, T_{Solidus} \right] \tag{3}$$

where V_f^γ presents the equilibrium volume fraction of γ matrix; T_γ^* is the critical temperature that the amount of γ reaches 80 % at solid state transformation; $T_{Solidus}$ stands for the equilibrium solidus temperature. These two types of cracking criteria are to subjected be optimized simultaneously to reach the AM processable compositions with low cracking susceptibility. All the calculations were performed by Thermo-Calc software using TCNI12 database.

Finally, the effect of MC / γ matrix interfaces was analyzed by post processing the potential solutions obtained. To this aim, the amount of primary carbides at solidus temperature, as well as the boron alloying

level of the candidate solutions, are calculated and recorded, which will be considered as the discriminating factor in the final alloy design routine. As mentioned in introduction section, former investigations have shown the possible correlation between the presence of MC carbides and the liquation cracking proneness. More specifically, Zhong et al. have reported that in laser deposited Inconel 738 alloy, (Ti, Ta)C carbides were observed to distribute coincidentally along liquation cracked grain boundary [41]. Also, the liquated γ/γ' eutectic phases were commonly detected to form at the vicinity of TiC carbides, which were generally observed as the vulnerable regions for crack initiation and propagation [35,36]. Although current researches struggle to clarify the exact relationship between the formation of (Ti,Ta)C carbides and the liquation cracking, the TiC/TaC-type MC carbides are temporarily not considered in this design routine for prudence, while the NbC carbide is selected as the target phase thereby. Correspondingly, the utilization of NbC / γ phase boundary will be implemented in the alloy design routine.

2.3. Results produced by the model

By employing the alloy design model, more than 10^7 composition candidates are calculated following the design strategy. Around 3000 desirable solutions that meet all the constraint factors are obtained, with their target features being recorded and shown in Fig. 2. Following the strategy of introduced phase boundary, the solutions with/without primary carbides are categorized, and indicated by the round and square symbols, respectively. The color of the symbols reflects the boron level. The colors are found to be distributed rather randomly over the whole scale range of potential solutions, indicating a weak correlation between the boron concentration and employed crack susceptibility criteria (assuming the underlying thermodynamic data to be sufficiently correct to reflect the impact of minor amounts of B). The optimization routines to achieve the printability are implemented by minimizing the freezing range as the hot crack susceptibility, and reducing the SAC factor as the strain-age crack proneness simultaneously. The "Pareto fronts" are thereby constructed as the trade-off surface of the optimal combination of freezing range and SAC criteria, which are marked by the black dash lines. The solutions along the front are highlighted by darker edge as the decent combination of FR and SAC depending on the nature of the two properties. For the carbide-containing category, the best combination of
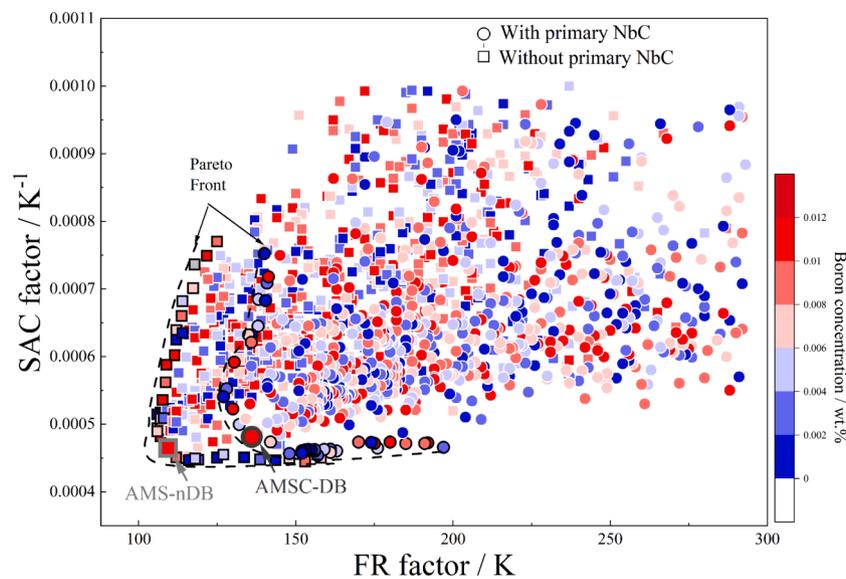
Fig. 2. The distribution of all desirable solutions qualified for pre-screening plotted in the domain of strain-age crack susceptibility (SAC factor) and freezing range (FR factor), with the circles and squares representing the categories with and without primary carbides, respectively. Their colours correspond to the nominal concentration of boron.

FR and SAC can be found at the turning point of the Pareto front, indicated by the black arrow, which is labelled as AMSC-DB alloy (Additive Manufacturable Superalloys with Carbide to Distributing boron). The alloy labelled as AMS-nDB alloy (Additive Manufacturable Superalloys with no Distribution of boron) in the carbide-free group was selected. Besides, it is still interesting to point out that according to the two screening parameters imposed (not taking into account any inhomogeneity in the spatial B distribution) the composition without carbides should perform better than the composition with carbides, as the Freezing Range values is substantially lower, while the SAC values are more or less comparable.

It is noteworthy that we are not claiming the model to be robust, since the composition with "best" printability can only be theoretically found when spending infinite computing time. The design model based on simple scalar parameters cannot capture the 'objective optimum', but only give a best estimated point to initiate actual printing experiments.

3. Experimental materials and methods

3.1. Alloy compositions and AM processing parameter space

The powders of the two newly designed alloys, AMS-nDB and AMSC-DB, were prepared by vacuum induction melting and argon gas atomization, while the actual chemical compositions of these alloys were determined by inductively coupled plasma-optical emission spectroscopy, as shown in Table 2. The comparison of the chemical composition of the two newly designed alloys and existing Ni commercial systems using a Principle Component Analysis is shown in Fig. S3 in Supplementary Materials. The figure shows that there is no composition similar to the new compositions, indicating the effectiveness of the design model in searching for new compositional domains for printable superalloys. The detailed characterization of powder morphology and size distribution is presented in next section.

An AM system equipped with an ytterbium fiber laser source was employed to produce alloy bulk samples. The scanning strategy was chosen to be 67° Rot-scan, indicating the scanning vector rotates 67° between each adjacent layer. To explore the direct laser deposition (DLD) processing window to produce near fully dense bulk samples, more than 40 sets combinations of printing parameters were applied with variation in laser power, laser scanning speed and hatching space. The parameter ranges are listed in table 3. The volumetric energy density Ev reflecting the energy imparted to the powder in the unit volume was calculated by $E_V = P/h\ v\ d$, where P is laser power, h is the hatching space, v is laser scanning speed and d is the layer thickness. All prints were conducted under the high purity argon atmosphere.

3.2. Thermo-mechanical testing

A STA449F3 type Differential Scanning Calorimeter (DSC) was used to measure the solidification behavior of alloys. Around 30 mg of powder was placed in the alumina crucibles. A flowing argon atmosphere (20 ml/min) was applied during the measurements. Samples were heated to 1450 °C, then the heat flux was recorded at an imposed cooling rate of 10 °C /min to 700 °C.

Cubes with dimensions of $10\times10\times10$ mm^3 were printed for microstructural characterization, while $16\times16\times60$ mm^3 cuboids were fabricated for mechanical testing, with the long side being the building direction. The tensile dog-bone samples were cut and machined into tensile samples with a gauge diameter of 3 mm and a gauge length of 20

mm with the longitudinal axis parallel to the building direction. Samples were taken from the centre of the printed samples to exclude edge effects. The surfaces of tensile samples were ground and polished up to 1200 grits sand papers. The tensile tests of as-printed sample were performed at ambient temperature and at a strain rate of $10^{-3}\ s^{-1}$. For the tensile tests performed at high temperatures, the heating rate to the testing temperature was set to 50 K/s, while the strain rate was increased to $10^{-2}\ s^{-1}$ to minimize possible annealing effects. All high temperature tests were conducted in air and at least three samples were tested per condition.

A SETARAM S60 type thermo-gravimetric analysis (TGA) was used to assess the oxidation resistance of the as-printed samples. Specimens of dimensions 10 mm × 10 mm × 1 mm were cut perpendicular to the build direction and polished to a mirror finish with 5000 grit sand paper. The tests were carried out in 5 steps, initially a protective Ar gas was run for 1 h to ensure equilibrium of the system. This was followed by an increase in temperature at a rate of 20 K/min to the test temperature of 1000 °C which was then followed by a hold for 30 min under protective Ar and then the onset of the oxidizing laboratory air flow at a rate of 50 ml/min for 24 h. After this period the sample is cooled to room temperature at 20 K/min. The evolution of mass gain was analyzed starting at the onset of oxidizing air.

3.3. Microstructural characterization

The as-printed cube samples were wire-cut into halve along and perpendicular to the building direction, and the intersections were ground, polished and finished with vibration polishing using 50 nm colloidal silica. The metallographic images of as-printed samples were taken by the Leica DM6 Optical Microscopy (OM). The defects area fraction of the binarized OM images were quantified by the ImagePro software to balance the statistical representativeness and precision. The samples with no detectable cracks are defined as "low-defect-density" samples, since the defects with the size smaller than 1 μm are beyond the characterization capability and generally not considered [14,47]. The crystallographic microstructural features were characterized using a Zeiss Gemini 300 scanning electron microscope (SEM) equipped with an electron backscatter diffraction (EBSD, Oxford Instruments). The EBSD data was post-processed using the Aztec Crystal 2.0 analysis software, with indexing rates greater than 99 %. Secondary Ion Mass Spectrometry (SIMS) analyses were carried out with a PHI nano Time-of-Flight (ToF) SIMS. The instrument was operated with a Bi_3^{2+} primary ion beam, while the boron distribution was investigated using the secondary ion species $^{11}BO^{2-}$. To study specific sites of crack tips and carbide vicinity, a focused ion beam (FIB) plan-view sample preparation technique was used. Transmission electron microscopy (TEM) and electron energy loss spectroscopy (EELS) were conducted using an FEI Titan G2 objective aberration corrected TEM operated at 300 kV with a Gatan Quantum image filter. EELS line scan were created by integrating the EELS signal of each edge: B, K (188 eV) and C K (284 eV), over a suitable energy window after subtracting the preceding exponential background fitted

Table 3
The ranges of printing processing parameters used in this study (layer thickness: 0.6 mm).

Laser Power, P / W	Laser scanning speed, v / mm.s^{-1}	Hatching space, h / mm	Volumetric energy density, E_V / J.mm^{-3}
900–1600	4–14	1.2–2.0	80–200

Table 2
Alloy compositions of newly designed alloys (in wt.%).

	Al	Co	Cr	Mo	Ta	Ti	W	C	B	Nb	Ni
AMS-nDB	6.44	13.8	5.05	0.06	0.67	0.03	4.48	0.2	0.02	0.17	Bal.
AMSC-DB	6.24	14.6	5.95	0.03	0.97	0.02	2.25	0.2	0.02	2.1	Bal.

with a power law.

4. Results

4.1. Solidification features

The DSC thermograms acquired during the cooling cycles of newly designed alloys are shown in Fig. 3(a)and (d). The cooling curves from 1450 °C to 700 °C reflect the features of solidification and phase transformations. The values of the transformation temperatures measured are listed in the inserted tables. For AMS-nDB alloy, only one exothermic peak appears during solidification corresponding to the freezing of the gamma matrix present. In contrast, for AMSC-DB alloy, an additional peak can be observed besides the matrix solidifying, confirming the formation of primary precipitate in melt. Although it is impossible to replicate the cooling rates of the AM process in DSC, the current results partially validate the design strategy for carbide-free AMS-nDB alloy and carbide-containing AMSC-DB alloy. Besides, very sharp onsets of solidification with narrow equilibrium freezing ranges can be found for the two new alloys. The liquidus temperature for AMS-nDB and AMSC-DB alloys are 1402 °C and 1384 °C, respectively, and the γ' formation temperatures identified as the change in heat flow were similarly around 1130 °C for these two alloys.

The powder size and powder morphology have also been checked for consistency. The two powders are both found to exhibit a near-spherical external morphology with only a few satellite particles, see Fig. 3(b) and (e). The powder size distributions are very similar as shown by the distribution curves (differential and cumulative) in Fig. 3(c) and (f). The D10, D50 (median), D90 values of the powders distributed around 48 μm, 97 μm and 173 μm, respectively, as given in the inserted table. The identical distribution of powder size can thereby exclude the influence of powder features, while it is the alloy composition which influences the processability.

4.2. Determination of optimal processing parameters

To determine the best processing parameters for fabricating AMS-nDB and AMSC-DB alloys with minimum defects level, a large spectrum of printing parameters have been employed (as listed in table 3), and an array of 36 samples were printed for each alloy. The as-printed samples were wire-cut in half parallel to the building direction.

Optical microscopy images of intersections were taken, and the defect features were quantitatively recorded, with the raw data shown in table S5 in Supplementary Materials. The defects observed in this work mainly fall into two categories, i.e., microcracks with a wavy morphology, and the spherical pores. The area fractions of the two defect types are shown in the bubble plots, while the background contours indicate the distribution of printable parameters. The corresponding optical micrographs of the best and worst printed samples were selected to present the distribution and morphologies of defects at low magnification, where the cracking and porosity are marked by black and grey arrows respectively.

As indicated in Fig 4, microcracks are the dominate type of defects in the AMS-nDB alloy, which occupy a much larger areal fraction than the pores. The optimal printable parameters are located in the map at conditions leading to small bubbles with the blue background (i.e., low areal fraction). From Fig. 4(a), it can be deduced that the optimal printing parameters tend to crowd in the region where the laser power and volumetric energy density are both at a high level. Increasing the processing input energy with a reduced printing speed will help to achieve better intactness of bulk samples. The smallest and biggest bubbles that reflecting the best and worst processing parameters are accordingly pointed by a red and a blue arrow respectively, and the digitized optical micrographs are shown in Fig. 4(c) and 4(d) respectively. In Fig. 4(c), the lowest defect area fraction of 0.12 % in total can be obtained for a combination of laser power 1500 W and a volumetric energy density 198.3 J/mm^3, leading to a few pores and sparsely distributed micro-cracks. On the other hand, micro-cracking with a wavy morphology is much more pronounced when applying the most unfavorable printing parameters in Fig. 4(d). In such a case the total area fraction of defects attains a value 2.2 %.

In contrast, the defect formation behavior is quite different for AMSC-DB samples. As shown by the bubble plots in Fig. 4(e) and 4(f), no detectable micro-cracks are observed throughout, reaching the low-defect-density bulks over the whole processing domain. Meanwhile, only a small number of porosity are present with the total pore area fractions well below 0.2 %. Compared to AMS-nDB alloy, the entire blue region in 4(e) indicates a very wide processing window for the AMSC-DB alloy. Fig. 4(g) shows that the near-defect free bulk sample can be obtained as combination of printing parameter of 1500 W and 161 J/mm^3, while the defect area fraction can be kept as low as 0.03 %. Even for the sample with highest defects fraction in Fig. 4(h), only a few numbers of
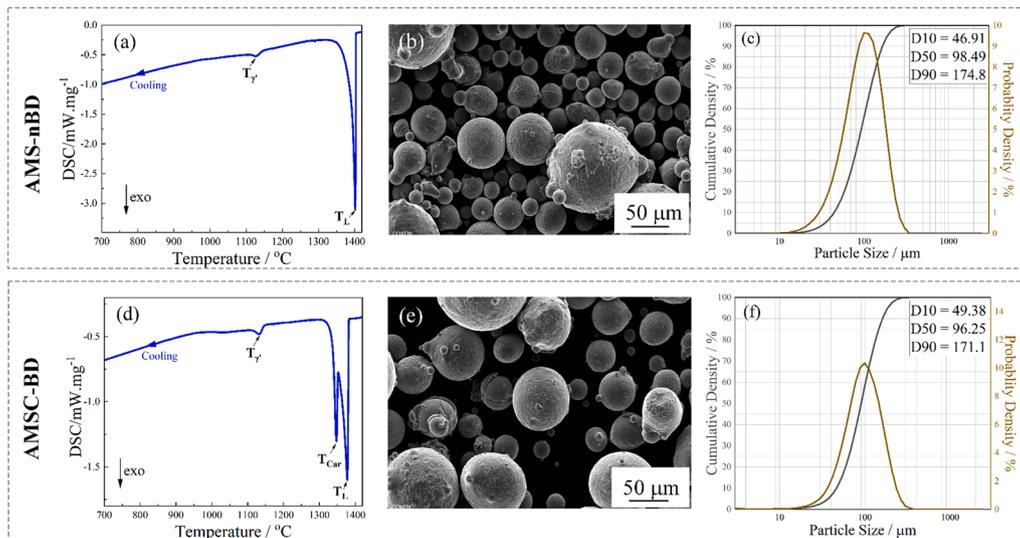
Fig. 3. Differential scanning calorimetry (DSC) curves obtained for the AMS-nDB and AMSC-DB alloys during cooling at 10 K/min (a, d). T_L, T_{Car} and $T_{\gamma'}$ represent the temperatures of liquidus, precipitation of carbide and formation of γ', respectively. The SEM images of the powders (b, e) and the corresponding powder size distribution (c, f).
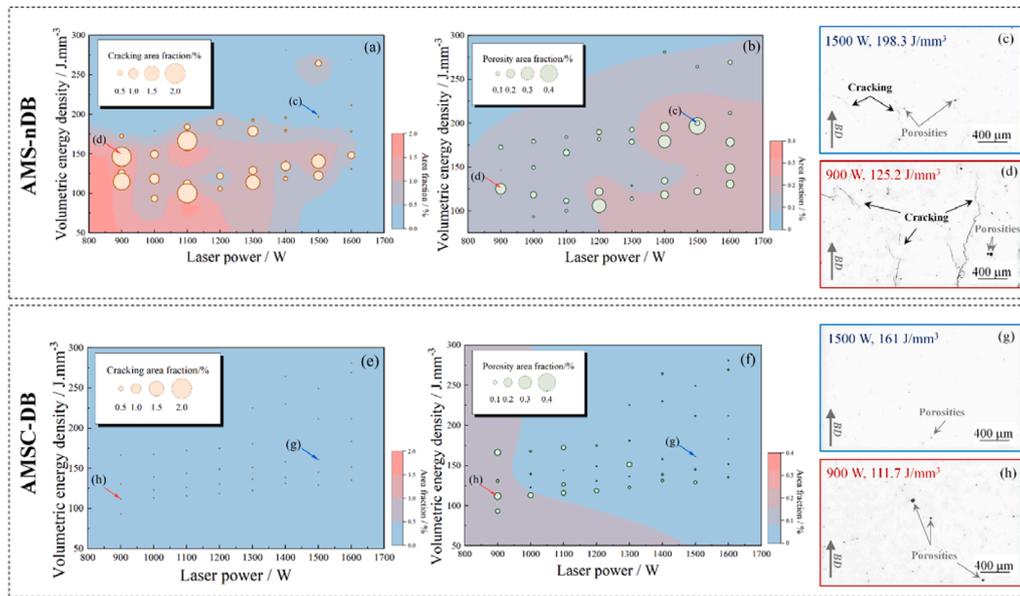
Fig. 4. The bubble plots showing the area fraction of cracking and porosity in AMS-nDB alloy(a, b) and AMSC-DB alloy(e, f) over a wide spectrum of laser power and volume energy density, while the background contours indicate the distribution of printable parameters. The optical micrographs show the samples with lowest defects fraction and highest defects fraction for AMS-nDB alloy(c, d) and AMSC-DB alloy(g, h), respectively. Conditions marked (c) and (g) mark the optimal printing conditions for AMS-nDB and AMSC-DB respectively.

pores are observed, with the defect fraction around 0.17 %. The favorable intactness of the as-printed bulk samples and the high robustness in processing parameters confirm the intrinsic excellent printability of the AMSC-DB alloy.

The defect area fractions for the new alloys are compared with those of existing printable Ni superalloys produced at their own optimal printing parameters [18,47-53], and the results are shown in Suppl. Fig. S6. It is found that the defect area fractions for the new alloys are generally at a low level compared to their commercial counterparts. The AMS-nDB alloy possesses the high intactness which can well outperform the weldable grades Inconel 718, while the defect fraction of AMSC-DB is comparable to solution strengthened grades Inconel 625. The excellent fabricability of the newly designed alloys nicely confirms the effectiveness of the hybrid design model.

The determined optimal processing parameters for AMS-nDB and AMSC-BD alloys were thereby adopted as the fabricating conditions for the subsequent sample preparation for microstructural and mechanical characterization. The defect formation behavior induced by processing

parameters can be excluded to a large extent, such that dominating effects on crack behaviors can be ascribed to the chemical compositions of both alloys.

4.3. The microstructure of as-fabricated alloys

Characterization of the cross section of as-printed samples has been made to capture the microstructure features of newly designed alloys. Fig. 5(a-d) shows the SEM micrographs of AMS-nBD alloy parallel and perpendicular to the building direction, while the dendritic core (DC) regions and interdendritic (ID) regions are marked by light and dark yellow arrows, respectively. The microcracks and pores are marked by the white arrows and they are generally distributed in interdendritic regions. Besides, a semi-continuous phase with a film-like morphology is observed at some grain boundaries. Micro-cracks are detected to initiate and propagate along the (sub-) grain boundaries. To better characterize the cracking features, the SEM-BSE images of cracked regions with higher magnification are presented in Fig. 5(b) and 5(d). Of particular
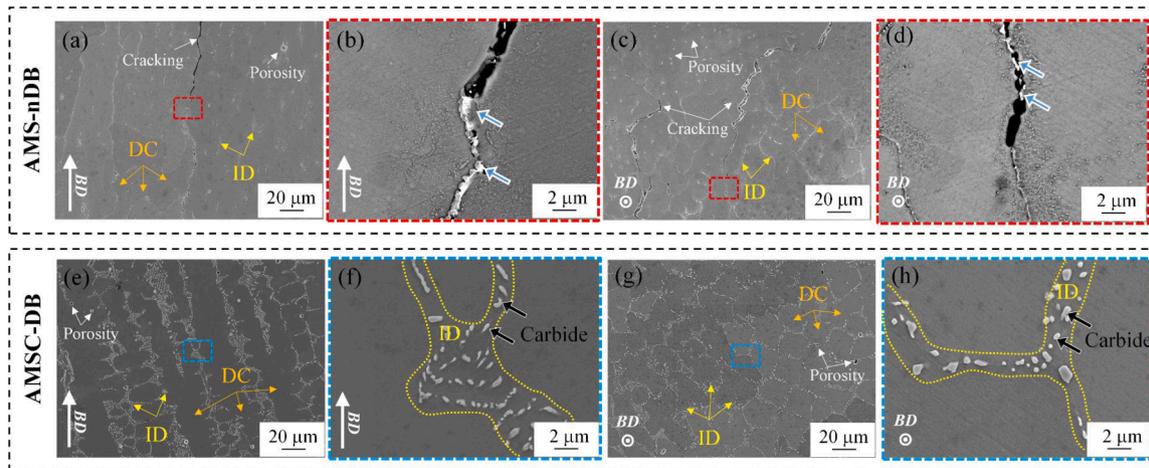
Fig. 5. Microstructure of the as-printed samples observed in the central part of the cross section parallel and perpendicular to the building direction. The SEM micrographs showing the corresponding etched samples in two magnifications for AMS-nDB alloy (a-d) and AMSC-DB alloy (e-h), respectively.

interest is that the cracks exclusively show the typical features of liquation cracking [5], where the presence of film shape phases agrees well with the liquated regions, as shown by the white features in Fig. 5 (b) and 5(d). The detailed characterization of the film shape phases will be presented in the next section.

SEM micrographs of AMSC-DB alloy are shown in Fig. 5(f-i). From the microstructural features of the vertical and horizontal cross sections, it can be clearly seen that the interdendritic regions of AMSC-DB alloys contain a high density of well distributed precipitates. Compared to the microstructure of AMS-nDB alloys, no film shaped phase is present, with only a few pores distributed at interdendritic regions in the vicinity of particles. The interdendritic precipitates are identified as MC carbides based on the XRD results provided in Suppl. Fig. S7. The area fraction of the MC precipitates in the as-printed microstructure is around 5.5 %, confirming the intended high level of surface areas of phase boundaries.

Fig. 6(a) shows the EBSD-inverse pole figure (IPF) maps of AMS-nDB alloy, where the coloring reference shows a slightly ⟨001⟩ orientation preference. The higher magnification of cracked region marked by the white frame is shown in Fig. 6(b), which shows the overlap of the EBSD-band contrast (BC) map and the Grain Boundary (GB) plots. The low angle grain boundaries (LAGB, misorientation between 2° and 15°) and high angle grain boundaries (HAGB, misorientation > 15°) are marked by light and dark blue, respectively, and the cracked regions are indicated by white arrows. It is found that cracking takes place exclusively along the HAGBs, while the LAGBs remain uncracked. Such observations agree well with results reported in the literature [15,33,54]. Fig. 6(c) shows the EBSD-IPF map of AMSC-DB alloy, which exhibits a strong ⟨001⟩ fiber texture parallel to the building direction. Compared to the microstructural features of AMS-nDB alloy in Fig. 5(a) and Fig. S7, the presence of primary carbides distributed in the interdendritic regions may promote some mechanical anisotropy for the as-printed microstructure.

Former studies have proved that HAGBs are more prone to cracking for AM Ni superalloys [15,33,54]. Meanwhile, it has also been widely reported that the refined grains help to reduce the crack susceptibility, since the enlargement in grain boundary area helps to mitigate the element segregation and local concentration of thermal stresses [33,55,56]. The grain features for the new alloys have been compared and are presented in Fig. 6(d). For AMS-nDB alloy, the HAGBs occupies 86.4 % of the total grain boundaries. Meanwhile, quite comparable fraction in

AMSC-DB alloy can be observed with the value around 82.2 %. On the other hand, the average grain sizes of AMS-nDB and AMSC-DB samples are 235.5±97.9 um and 465.1±143.4 um, respectively. The AMS-nDB alloy possesses a similar fraction of HAGBs but with finer grains, which was supposed to present better printability compared with AMSC-DB alloy. The observations indicate that the grain misorientation and grain sizes determined by the processing parameters and in particular the local transient thermal conditions, are largely not the dominating influencing factors for printability.

4.4. Element segregation behaviors

The distribution of B, C and Nb in AMS-nDB alloy and AMSC-DB alloys at the mesoscopic scale as measured by ToF-SIMS are shown in Fig. 7. Pre-sputtering of sample surface was performed before each measurement in order to minimize O and C surface contamination. The different images, one for each type of ion, over this field of view of 100 × 100 μm^2 were acquired simultaneously. To compare the segregation behavior in these two alloys, the color codes for corresponding elements (quantified by the contour bar) have been made equal enable intermaterial comparison. Significant segregation of boron atoms along cracking can be detected in Fig. 7(a). The morphology of boron rich region agrees well with the intergranular phases along cracks in Fig. 5, which confirms that the semi-continuous films are boron-rich phases acting as the origin of liquation cracking. C signal is depleted in the vicinity of cracks, and no detectable carbon clustering was observed (Fig 7b). Meanwhile, Fig 7(c) shows that the Nb signal can be barely detected due to the low alloying level, in line with the intended absence of carbides in AMS-nDB. In contrast with AMS-nDB alloy, the AMSC-DB alloy possess the identical boron concentration (in Table 2). However, results in Fig. 7(d) clearly show an even mesoscopic boron distribution with no detectable spatial enrichments. Besides, the regions of high concentrations of C and Nb were found to overlap in Fig. 7(e) and 7(f), indicating the formation of NbC carbides. The great difference in boron distribution in carbide-free and carbide-containing alloys is highly coupled with the difference in micro-crack behavior, indicating the dominant effect of boron atoms on the crack susceptibility.

The film shape precipitates along the crack path in AMS-nDB alloy are further characterized by TEM. The site-specific lamellar sample was lifted out at the crack tip (shown in Suppl. Fig. S9). The scanning
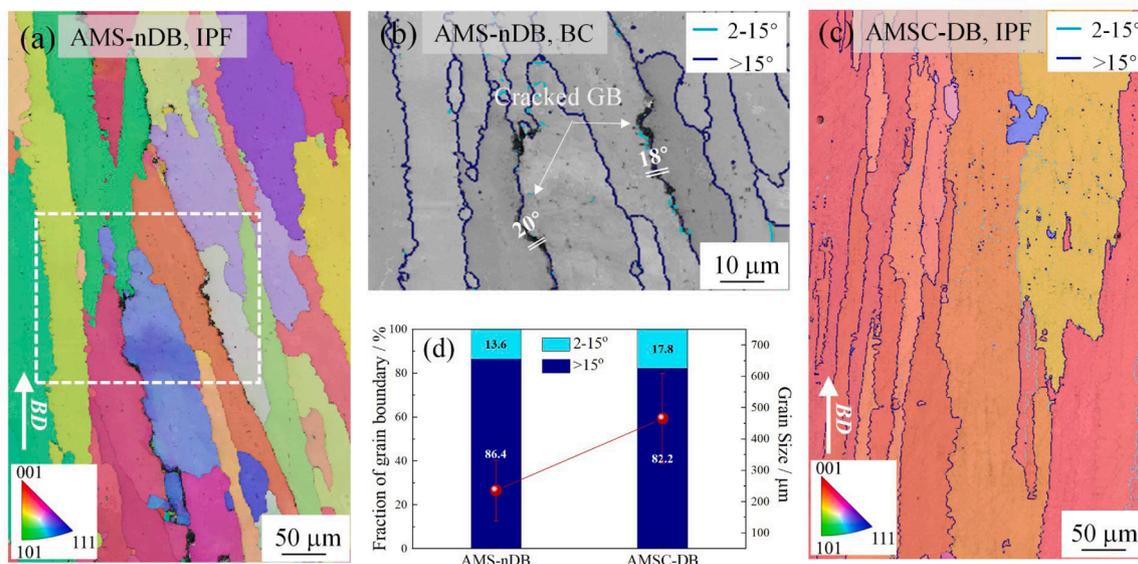
Fig. 6. The EBSD-IPF image of AMS-nDB alloy (a) and the EBSD-BC map overlapped with GB plots in the white box area (b); the EBSD-IPF image overlapped with GB plots of AMSC-DB alloy (c); the fraction of grain boundaries with low (2–15°) and high (>15°) misorientation, and corresponding grain sizes for AMS-nDB and AMSC-DB alloys(d).
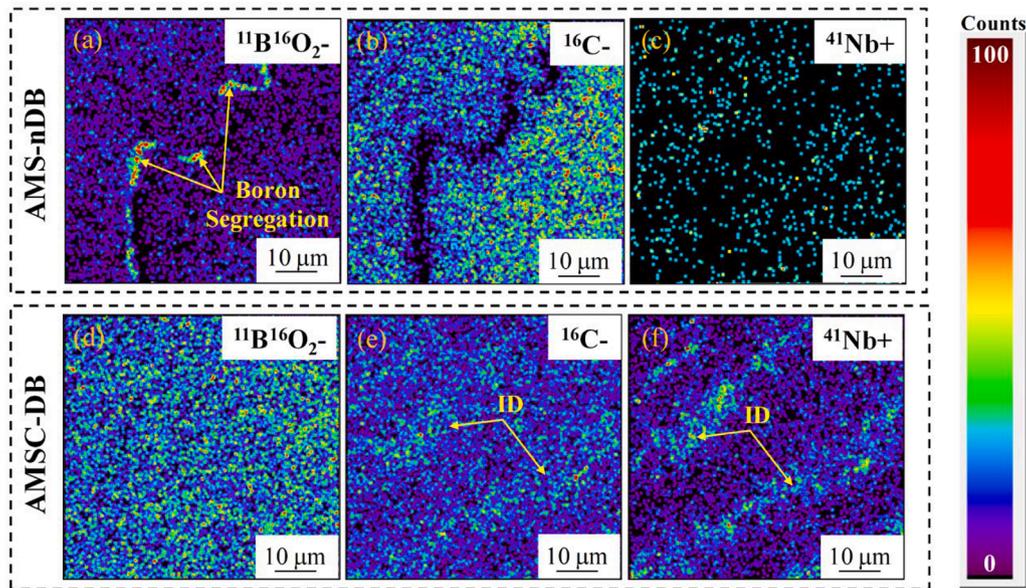
Fig. 7. ToF-SIMS images showing the B, C, Nb element distribution behavior of AMS-nDB alloy(a-c) and AMSC-DB alloy(d-f), respectively.

transmission electron microscopy (STEM) high-angle annular dark field (HAADF) image of a precipitate and the corresponding elemental maps are shown in Fig. 8(a). The precipitate detected is highly enriched in Cr, and poor in Ni, Al, C and Ta. To further identify the boron distribution in the target precipitate, the EELS line scan was conducted along the red line in Fig. 8(a), where the relative intensities of boron and carbon atoms were normalized with respect to their elemental scattering cross sections, so that they can be directly related to the number of atoms along the electron beam. The EELS profile is shown in Fig. 8(b). A sharp

increase in boron intensity along the precipitate/matrix interface has been detected, confirming the strong boron enrichment in the precipitates. High-resolution image centered on the phase boundary is given in Fig. 8(c), while the selected area diffraction (SAD) patterns in the insets were obtained from the precipitates and matrix respectively. By indexing these SAD patterns, the precipitate was identified as Cr_2B boride with a tetragonal crystal structure. Current results were consistent with the formal investigations, where boron gets enriched and concentrated progressively during AM processing, until a critical
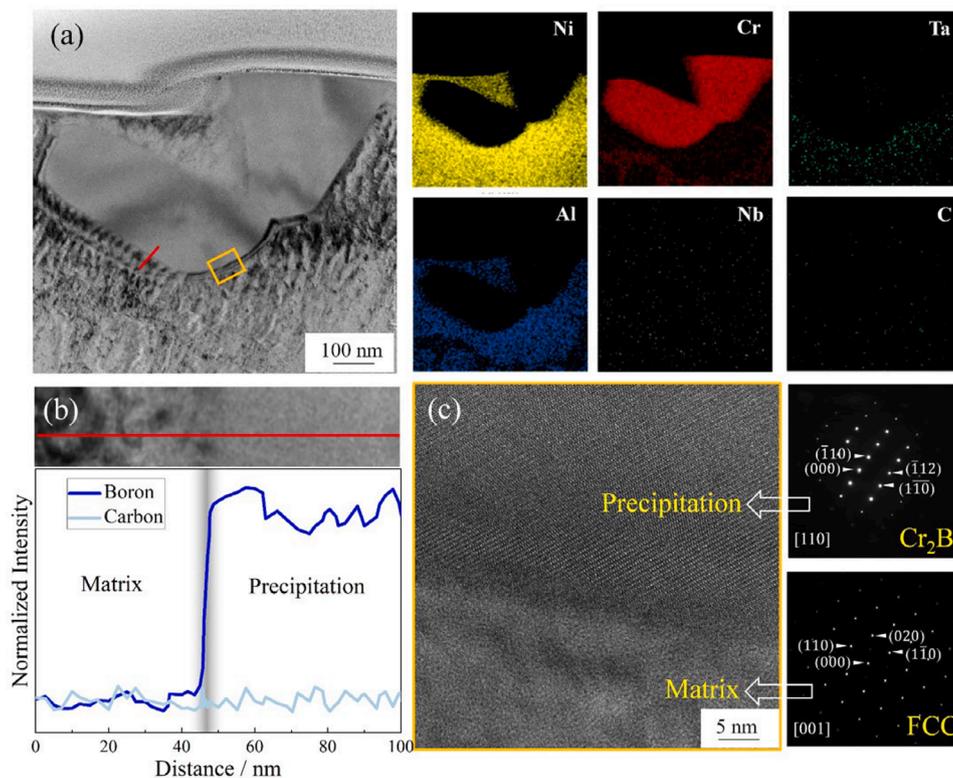
Fig. 8. TEM observations of film shape precipitates on the crack tip in AMS-nDB alloy. The STEM-HAADF image and the corresponding elemental maps of Ni, Cr, Ta, Al, Nb and C (a). The boron distribution obtained by EELS line-scan across the matrix/precipitate interface along the red line (b). The High-resolution TEM image centered on the matrix/precipitate interface, with inserts showing the electron diffraction patterns(c).

composition of boride-formers is finally reached and borides can nucleate [33]. It becomes apparent that the relatively high cracking susceptibility of AMS-nDB alloy originates from the uncontrolled boron segregation, where the presence of low melting point borides can easily lead to the grain boundary liquation and cause hot cracking.

To further detect the microscopic distribution of boron atoms in AMSC-DB alloy, the vicinity of MC carbides was characterized by TEM. Fig. 9(a) shows the STEM-HAADF image and corresponding elemental distribution maps. A strong enrichment of Nb can be detected, while no significant partition of other carbide forming elements, such as Ti, Mo and Ta, was observed. The EELS line scan was conducted along the red line in Fig. 9(b) while the phase boundaries of carbide / γ were characterized twice to detect the elemental distribution. Significant boron peaks can be detected at the carbide / γ interfaces, confirming the design strategy that distributing boron enrichment at carbide / γ phase boundaries. It is noteworthy that the boron enrichment at phase boundaries have been observed at multiple locations. The characterization results from another carbide site are presented in Fig. S10 in Supplementary Materials. Combined with the observed results in Fig 0.5, 7 and 8, it becomes apparent that the absence of low melting point borides and corresponding cracking in AMSC-DB can be attributed to the presence of MC/matrix phase boundaries. The larger total areas of phase boundaries in AMSC-DB alloy helps to better accommodate boron atoms and impede the uncontrollable of boron clustering at grain boundaries, thereby the critical composition for the formation of detrimental boride was prevented to be reached, and the cracking was inhibited correspondingly. High-resolution image centered on the phase boundary is given in Fig. 9(c), which indicates a near-coherent (100) interface with the face-centred cubic solid solution matrix. The electron diffraction patterns in the insets shows the crystal structure, confirming that the precipitate is a NbC carbide.
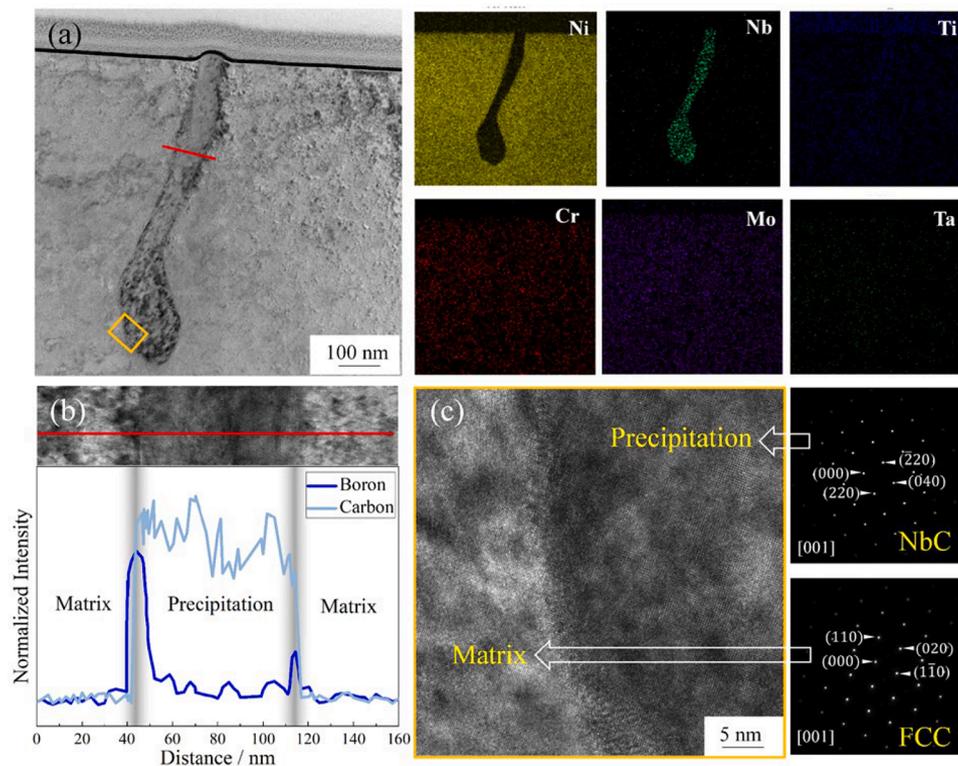
4.5. The mechanical properties of as-fabricated samples

Quasi-static tensile tests were carried out in order to study the mechanical response of the as-printed samples. Fig. 10(a) presents the ultimate tensile strength (UTS) and total elongation of as printed AMS-nDB and AMSC-DB alloys at different temperatures. At ambient temperature, minor difference in UTS and ductility between AMS-nDB and AMSC-DB can be observed. The values of UTS for AMS-nDB and AMSC-DB alloys remain comparable to each other at 800 °C and 900 °C with minor scatter. Regarding the elongation, AMSC-DB has a better ductility with less scatter at elevated service temperatures, which can be ascribed primarily to the low-defect-density matrix.

The comparisons of tensile properties with existing Ni alloys are made in Fig. 10(b-d). Square and tetragonal symbols represent data for conventionally processed Ni superalloys and existing printable Ni alloys, respectively. The red symbols mark the results for the newly designed alloys. The results in Fig. 10(b) show that the UTS of both new alloys at ambient temperature can achieve 1200 MPa, well above the level of commercial grades such as CM247LC and Rene41. At the minimal ductility temperature of 800 °C, the total elongation of AMS-nDB and AMSC-DB alloys can still outperform their commercials counterparts, with a strength level comparable to that of In939. At a temperature of 900 °C, a decent balance in strength and ductility can be observed for alloy AMSC-DB.

4.6. The oxidation resistance of as-fabricated samples

The thermo-gravimetric tests for newly designed alloys are done to evaluate the oxidation resistance of the newly designed alloys. The mass changes of AMS-nDB and AMSC-DB alloys were indicated by the solid lines in Fig 11(a), which were compared with that of existing Ni alloys presented by dash lines [62,63]. Results have shown that the AMSC-DB alloy exhibits the least mass gain possesses during the whole oxidation

Fig. 9. The TEM observations of carbides in AMSC-DB alloy. The STEM-HAADF image and the corresponding elemental maps of Ni, Nb, Ti, Cr, Mo and Ta (a). The boron distribution obtained by EELS line-scan across the matrix/precipitate interface along the red line (b). the High-resolution TEM image centred on the matrix/precipitate interface, with insets showing their electron diffraction patterns(c).

Fig. 10. The ultimate tensile strength and total elongation for AMS-nDB alloy and AMSC-DB alloy in as-printed states (a), and comparison of tensile properties with existing alloys at the temperature of (b) 25 °C, (c) 800 °C and (d) 900 °C [14,57-61]. The square and tetragonal symbols represent data for conventionally produced Ni superalloys and existing printable Ni superalloys, respectively.
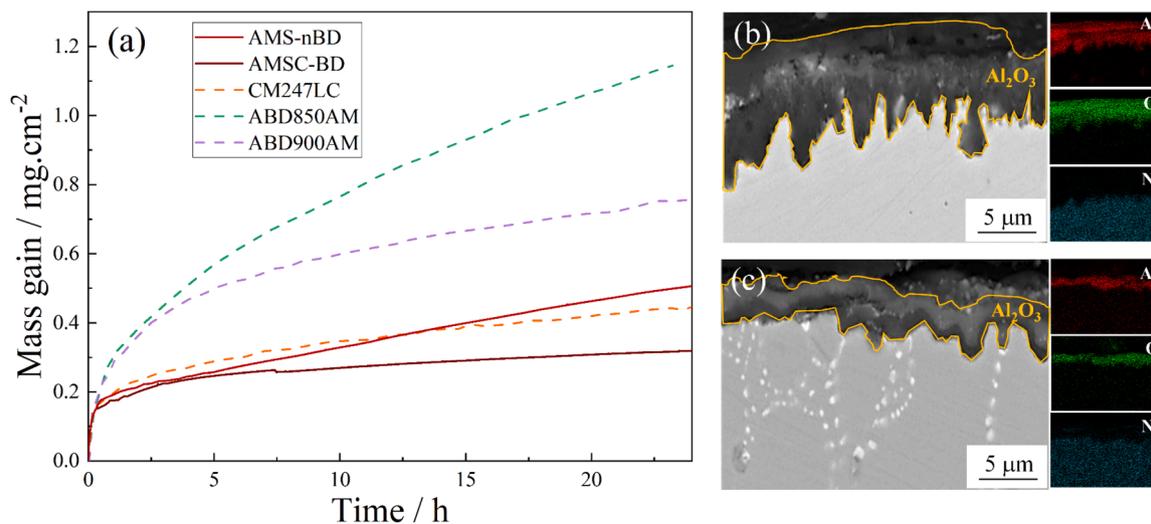
Fig. 11. The mass change of AMS-nDB alloy and AMSC-DB alloy during isothermal thermo-gravimetric testing at 1000 °C, and the comparison with existing alloys [62,63](a); BSE micrographs showing the oxide layers formed at the surface, and the corresponding EDX maps showing the distributions of elements for AMS-nDB alloy (b) and AMSC-DB alloy (c).

process, while the total mass gain after 24 h was 0.32 mg/cm², 28.8% less than that of CM247LC commercial alloy. AMS-nDB alloy shows similar oxidation behavior to AMSC-DB in the first 7 h, then gained mass more rapidly and slightly surpassed CM247LC alloy after 12 h. Namely, the newly designed AMSC-DB alloy and AMS-nDB alloy present decent oxidation resistance that can outperform or remain comparable to commercial alloy CM247LC.

The oxidation layers formed in each composition are shown in Fig 11 (b) and (c). BSE micrographs illustrate that the average thickness of the oxide layers are 4.6 μm and 2.1 μm for AMS-nDB alloy and AMSC-DB

alloy, respectively. The thin outer layers are detected as Al_2O_3 oxide layers in the EDX analysis. The exhibited continuous and stable Al_2O_3 oxide layers manage to offer adequate oxidation resistance, which is consistent with the low mass gain of the newly designed alloys. The decent oxidation resistance of AMS-nDB and AMSC-DB alloys nicely demonstrates the effectiveness in performance screening of the alloy design strategy.

5. Discussion

The above results demonstrate the high effectiveness of this hybrid design approach in designing novel Ni superalloys alloys with high robust printability and potentially decent service properties, while the strategy to employ phase boundaries to solve the boron segregation problems is experimentally validated as well. Nevertheless, the effectiveness and robustness of current results deserves some further rationalization, while the expansibility of the current scheme is also worth exploring.

5.1. The computational effectiveness of hybrid design model

The calculated properties of the two novel alloys, AMS-nBD and AMSC-BD based on their overall chemical compositions are plotted and compared with those of other existing Ni alloys in Fig. 12. The tetragonal symbols present the printable Ni alloys, while square symbols present commercial grades which have shown great cracking susceptibility during AM processing. As shown in Fig. 12(a), the black arrow points towards the printable alloys located at the left bottom corner, indicating that a lower crack susceptibility can be achieved by the combined minimization of freezing range and SAC. The newly designed alloys have the lowest values of FR and SAC metrics compared to their counterparts, confirming the efficiency of the current alloy design model for computing the specific compositions with target properties from a wide range of compositions (more than 10^7 as mentioned earlier). In Fig. 12 (b-c), the vertical and horizontal dashed lines present the threshold levels of the various constraints applied, and the patterned areas mark the forbidden regions where the requirements for good properties in case of an absence of printing defects are not fulfilled. All existing commercial Ni grades, such as CM247LC, In792 and In738LC (marked by squares) meet the constraint criteria set, validating the applicability of these constraints for mechanical strengthening effects, microstructural stability and oxidation resistance. The rationality of these preset constraints used in the model can be confirmed thereby. However, the criteria for minimum amount of γ' phases, minimum oxidation resistance, and maximum in undesirable phases are not well fulfilled by some of the printable alloys appeared on the market. For these alloys, a trade-off between service performance and manufacturability has been made. It should be pointed out that the AMS-nBD and AMSC-BD alloys are located in the permissible regions for each of the properties as shown in both Fig. 12(b) and (c). This means that computationally the newly designed alloys manage to balance an excellent additive manufacturability with good oxidation resistance and potentially decent mechanical properties.

5.2. The process robustness of newly designed alloy

The promising results reported thus far have confirmed the capability of the NbC / γ phase boundaries to tailor the B segregation behavior in the manner planned. In Fig. 4, a high amount of NbC carbides distributed at the interdendritic region of AMSC-DB alloy is observed when applying optimal printing conditions. Nevertheless, the remarkable high process robustness of AMSC-DB alloy for obtaining near-defect free bulk samples requires additional interpretation as well. To this aim, the microstructural features of the AMSC-DB alloys fabricated under various printing conditions were quantitatively characterized, and the area fractions of NbC carbide as a function of processing parameters have been obtained in Fig. 13. Fig. 13(a) shows that the fraction of NbC carbides remains rather stable over the full spectrum of processing parameters, and reaches a nearly constant level around 5.4 %. The corresponding microstructural images are shown in Fig. 13(b-e), which indicate that different volumetric energy densities cause variations in interdendritic arm spacings, yet have little effect on the fraction of NbC carbides (which form in the liquid state prior to solidification). The independence of carbide amounts on the processing parameters guarantees the presence of a large surface areas of NbC / γ phase boundaries irrespective of the process parameters, thereby leading to a high process robustness of AMSC-DB alloy.

It has to be mentioned that the quantitative tailoring of primary carbides was beyond the scope of the current design model, due to the limited understanding of the influence of introduced phase boundaries. In light of above results, quite a few questions demand further attention. For example, how the areas of target phase boundaries quantitatively influence the efficiency of elemental boron distribution, and whether there exists an optimal interval for the amount or the morphology for target phase boundaries to optimize the printability and mechanical properties. The above issues need to be addressed in future work.

5.3. The necessity to integrate design strategies

The necessity of the hybrid model in integrating the different design strategies was clarified in this section, where the computationally predicted and actual printability of AMS-nDB and AMSC-DB alloy are compared and analyzed. The design results in Fig. 3 show that the printability of AMS-nDB (calculated on the basis of overall chemical composition) was supposed to outperform AMSC-DB when neglecting the effects of elemental segregation in alloy design routine, since the values of optimization parameters of AMS-nDB alloy are consistently better than that of AMSC-DB alloy. Nevertheless, a relatively low process robustness and high defect fractions for AMS-nDB which suffers from cracking induced by boron-segregation has been observed, which should be compared to the low-defect-density AMSC-DB samples over a wide range of printable parameters, as presented in Fig. 4 and Fig. 5. Besides, the colors of the symbols (indicative of the boron level) in Fig. 3 are rather randomly distributed over the whole scale range, indicating effectively little correlation between the employed crack susceptibility criteria and boron alloying level. The above results have clearly proved
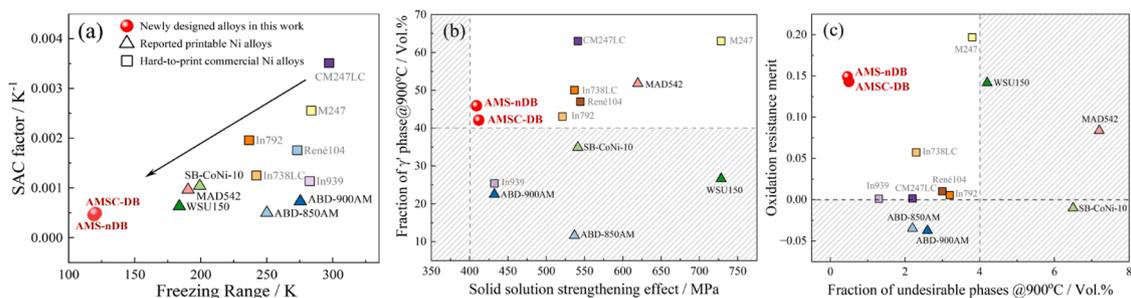
Fig. 12. The calculated properties of newly designed alloys and the comparison with existing Ni superalloys for (a) crack susceptibility criteria (b) γ' volume fractions and solid solution strengthening effects and (c) oxidation resistance and microstructural stability. The arrow in (a) indicates the design direction, while the dash lines and the patterned areas in (b-c) indicate the threshold level of the constraint criteria, and the forbidden regions where the requirements are not fulfilled, respectively.
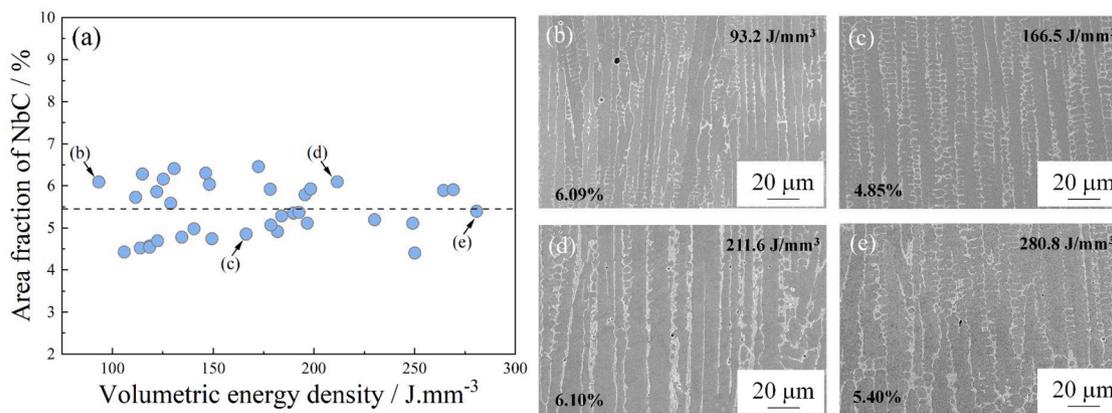
Fig. 13. The area fraction of NbC carbide as a function of volumetric energy density for AMSC-BD alloy (a), and the corresponding representative SEM micrographs (b-e).

that the boron segregation behavior and corresponding cracking susceptibilities can hardly be predicted by the thermodynamic calculations based on bulk average compositions. Meanwhile, the introduction of primary carbides can correspondingly strengthen the specific points of weakness and nicely output the well-performed AMSC-BD alloy. The necessity of the hybrid model in integrating different design strategies is confirmed hereby.

5.4. Potential of γ / MC phase boundaries in distributing other critical minor elements

It is worth noting that the employed phase boundaries of MC carbides and γ matrix have the potential to be further applied in distributing other critical minor elements such as Zr and Hf. The prospect has been preliminarily explored using first-principle calculations, and the segregation preferences of Zr and Hf atoms at MC (M=Nb, Ti) / γ phase boundaries have been simulated and are shown in Fig. S11 in Supplementary Materials. Negative segregation energies for Zr or Hf atoms at the substitutional sites near γ / MC interfaces have been obtained, indicating that γ/ MC phase boundaries provide preferable sites for Zr and Hf atoms to cluster. Experimentally, the enrichment of Zr atoms at γ / (Ti, Nb)C interface has been confirmed in Sun's work by employing atom probe tomography [16]. Further investigations are needed to address the feasibility and extendibility of target phase boundaries.

6. Conclusions

1. A novel strategy that introducing γ / MC phase boundaries to manipulate the uncontrollable segregation of critical minor elements has been proposed, while the feasibility of γ/ MC interface in trapping boron atoms was preliminarily verified by first-principle calculations, both for 0 K condition and for solidus temperature condition where boron partitioning is maximal.
2. By integrating the strategy to tune local elemental distribution with the scheme to minimize the cracking susceptibility using nominal chemical compositions, a hybrid design model has been developed to effectively design novel Ni superalloys with good printability and wide process window, as well as thermomechanical properties suggesting an attractive potential in real applications.
3. New alloy AMSC-DB has been developed as the combined consequence of the introduced γ / NbC phase boundary and optimized crack susceptibility criteria. The high robustness of processing parameters in fabricating low-defect-density bulk samples confirms its excellent manufacturability. No detectable mesoscopic clustering of boron was observed in AMSC-DB alloy, while boron atoms are detected to get enriched along matrix / NbC phase boundaries.

Therefore, the cracking induced by boron segregation in AMSC-DB alloy can be well inhibited.
4. The reference alloy AMS-nDB was also developed with no MC carbides but comparable cracking optimization parameters, which yielded relatively inferior, but still acceptable printability. Microcracks connected to the undesirable formation of Cr_2B borides along the interdendritic region were observed, due to the uncontrollable segregation of boron atoms in AMS-nDB alloy. The difference in printability between AMS-nDB and AMSC-DB alloys can well validate the feasibility of boron distributing strategy.
5. The newly designed AMSC-DB alloy showed decent balance in strength and ductility at room and elevated temperatures, as well as proper oxidation resistance, which are comparable to or better than conventionally produced superalloys.
6. The approach to employ phase boundaries to spatially manipulate the elemental distributions may have the potential to be applied to other critical minority elements as well, which may provide a new path for designing novel additive manufacturable Ni superalloys.

Declaration of competing interest

The authors declare that they have no known competing financial interests or personal relationships that could have appeared to influence the work reported in this paper.

Acknowledgments

Supplementary materials

Supplementary material associated with this article can be found, in the online version, at doi:10.1016/j.actamat.2024.119658.

References

[1] C. Panwisawas, Y.T. Tang, R.C. Reed, Metal 3D printing as a disruptive technology for superalloys, Nat. Commun 11 (2020) 2327.
[2] D. Gu, X. Shi, R. Poprawe, D.L. Bourell, R. Setchi, J. Zhu, Material-structure-performance integrated laser-metal additive manufacturing, Science 372 (2021) eabg1487.
[3] S.S. Babu, N. Raghavan, J. Raplee, S.J. Foster, C. Frederick, M. Haines, R. Dinwiddie, M.K. Kirka, A. Plotkowski, Y. Lee, R.R. Dehoff, Additive manufacturing of nickel superalloys: opportunities for innovation and challenges related to qualification, Metall. Mater. Trans. A 49 (2018) 3764–3780.
[4] X. Wang, L.N. Carter, B. Pang, M.M. Attallah, M.H. Loretto, Microstructure and yield strength of SLM-fabricated CM247LC Ni-Superalloy, Acta Mater 128 (2017) 87–95.

[5] E. Chauvet, P. Kontis, E.A. Jägle, B. Gault, D. Raabe, C. Tassin, J.-J. Blandin, R. Dendievel, B. Vayre, S. Abed, G. Martin, Hot cracking mechanism affecting a non-weldable Ni-based superalloy produced by selective electron Beam melting, Acta Mater 142 (2018) 82–94.

[6] Z. Zhou, L. Huang, Y. Shang, Y. Li, L. Jiang, Q. Lei, Causes analysis on cracks in nickel-based single crystal superalloy fabricated by laser powder deposition additive manufacturing, Mater. Des. 160 (2018) 1238–1249.

[7] S. Catchpole-Smith, N. Aboulkhair, L. Parry, C. Tuck, I.A. Ashcroft, A. Clare, Fractal scan strategies for selective laser melting of 'unweldable' nickel superalloys, Addit. Manuf. 15 (2017) 113–122.

[8] S.M.H. Hojjatzadeh, N.D. Parab, W. Yan, Q. Guo, L. Xiong, C. Zhao, M. Qu, L. I. Escano, X. Xiao, K. Fezzaa, W. Everhart, T. Sun, L. Chen, Pore elimination mechanisms during 3D printing of metals, Nat. Commun. 10 (2019) 3088.

[9] J. Hu, Y. Hu, C. Lan, Q. Zhang, F. Jin, W. Li, X. Lin, W. Huang, Cracking mechanism and control of Hastelloy X prepared by laser powder bed fusion, J. Mater. Res. Technol. 21 (2022) 3526–3547.

[10] A. Poudel, M.S. Yasin, J. Ye, J. Liu, A. Vinel, S. Shao, N. Shamsaei, Feature-based volumetric defect classification in metal additive manufacturing, Nat. Commun. 13 (2022) 6369.

[11] C. Li, P. Hodgson, M. Preuss, Y. Chen, X. Wu, Y. Zhu, Y. Tian, A. Huang, Rolling-assisted direct energy deposited Inconel 718: microstructural evolution and mechanical properties after optimized heat treatment, J. Mater. Sci. Technol. 144 (2023) 118–127.

[12] N.J. Harrison, I. Todd, K. Mumtaz, Reduction of micro-cracking in nickel superalloys processed by Selective Laser Melting: a fundamental alloy design approach, Acta Mater 94 (2015) 59–68.

[13] S.P. Murray, K.M. Pusch, A.T. Polonsky, C.J. Torbet, G.G.E. Seward, N. Zhou, S.A. J. Forsik, P. Nandwana, M.M. Kirka, R.R. Dehoff, W.E. Slye, T.M. Pollock, A defect-resistant Co-Ni superalloy for 3D printing, Nat. Commun 11 (2020) 4975.

[14] Y.T. Tang, C. Panwisawas, J.N. Ghoussoub, Y. Gong, J.W.G. Clark, A.A.N. Németh, D.G. McCartney, R.C. Reed, Alloys-by-design: application to new superalloys for additive manufacturing, Acta Mater 202 (2021) 417–436.

[15] A. Hariharan, L. Lu, J. Risse, A. Kostka, B. Gault, E.A. Jägle, D. Raabe, Misorientation-dependent solute enrichment at interfaces and its contribution to defect formation mechanisms during laser additive manufacturing of superalloys, Phys. Rev. Mater. 3 (2019) 123602.

[16] Z. Sun, Y. Ma, D. Ponge, S. Zaefferer, E.A. Jägle, B. Gault, A.D. Rollett, D. Raabe, Thermodynamics-guided alloy and process design for additive manufacturing, Nat. Commun. 13 (2022) 4361.

[17] H. Yu, J. Liang, Z. Bi, J. Li, W. Xu, Computational design of novel Ni Superalloys with low crack susceptibility for additive manufacturing, Metall. Mater. Trans. A 53 (2022) 1945–1954.

[18] J. Xu, P. Kontis, R.L. Peng, J. Moverare, Modelling of additive manufacturability of nickel-based superalloys for laser powder bed fusion, Acta Mater 240 (2022) 118307.

[19] A. Shukla, S. Sarkar, A. Durga, R. Adharapurapu, L. Dial, S.K. Sondhi, et al., Computational design of additively printable nickel Superalloys, in: S. Tin, M. Hardy, J. Clews, J. Cormier, Q. Feng, J. Marcin, et al. (Eds.), Superalloys, Springer International Publishing, Champion, 2020, pp. 1066–1074, 2020.

[20] J.C. Lippold, S.D. Kiser, J.N. DuPont, Welding metallurgy and weldability of nickel-base alloys, John Wiley & Sons (2011).

[21] M. Rappaz, J.M. Drezet, M. Gremaud, A new hot-tearing criterion, Metall. Mater. Trans. A 30 (1999) 449–455.

[22] T. Clyne, G. Davis, The influence of composition on solidification cracking susceptibility in binary alloy systems, Br. Foundrym. 74 (1981) 65–73.

[23] Y. Zhao, Z. Ma, L. Yu, Y. Liu, New alloy design approach to inhibiting hot cracking in laser additive manufactured nickel-based superalloys, Acta Mater 247 (2023) 118736.

[24] Z. Sun, X. Tan, C. Wang, M. Descoins, D. Mangelinck, S.B. Tor, E.A. Jägle, S. Zaefferer, D. Raabe, Reducing hot tearing by grain boundary segregation engineering in additive manufacturing: example of an AlxCoCrFeNi high-entropy alloy, Acta Mater 204 (2021) 116505.

[25] D. Tomus, P.A. Rometsch, M. Heilmaier, X. Wu, Effect of minor alloying elements on crack-formation characteristics of Hastelloy-X manufactured by selective laser melting, Addit. Manuf. 16 (2017) 65–72.

[26] K. Lindgren, F. Schulz, H. Gruber, A. Markström, E. Hryha, On the role of Zr and B addition on solidification cracking of IN738LC produced by laser powder bed fusion, Materialia 26 (2022) 101607.

[27] J. Grodzki, N. Hartmann, R. Rettig, E. Affeldt, R.F. Singer, Effect of B, Zr, and C on hot tearing of a directionally solidified nickel-based superalloy, Metall. Mater. Trans. A 47 (2016) 2914–2926.

[28] M. Montazeri, F.M. Ghaini, The liquation cracking behavior of IN738LC superalloy during low power pulsed Nd:YAG laser welding, Mater. Charact. 67 (2012) 65–73.

[29] P. Kontis, H.A.M. Yusof, S. Pedrazzini, M. Danaie, K.L. Moore, P.A.J. Bagot, M. P. Moody, C.R.M. Grovenor, R.C. Reed, On the effect of boron on grain boundary character in a new polycrystalline superalloy, Acta Mater 103 (2016) 688–699.

[30] B.C. Yan, J. Zhang, L.H. Lou, Effect of boron additions on the microstructure and transverse properties of a directionally solidified superalloy, Mater. Sci. Eng. A 474 (2008) 39–47.

[31] F. Deirmina, S. Koenig, M. Hasselqvist, E. Oscarsson, O. Adegoke, N.H. Pettersson, M. Pellizzari, Influence of boron on the stress-rupture behavior of an additively manufactured Hastelloy X, Mater. Sci. Eng. A 863 (2023) 144483.

[32] M. Kolb, L.P. Freund, F. Fischer, I. Povstugar, S.K. Makineni, B. Gault, D. Raabe, J. Müller, E. Spiecker, S. Neumeier, M. Göken, On the grain boundary strengthening effect of boron in γ/γ′ Cobalt-base superalloys, Acta Mater 145 (2018) 247–254.

[33] P. Kontis, E. Chauvet, Z. Peng, J. He, A.K. da Silva, D. Raabe, C. Tassin, J.-J. Blandin, S. Abed, R. Dendievel, B. Gault, G. Martin, Atomic-scale grain boundary engineering to overcome hot-cracking in additively-manufactured superalloys, Acta Mater 177 (2019) 209–221.

[34] A. Després, C. Mayer, M. Veron, E.F. Rauch, M. Bugnet, J.J. Blandin, G. Renou, C. Tassin, P. Donnadieu, G. Martin, On the variety and formation sequence of second-phase particles in nickel-based superalloys fabricated by laser powder bed fusion, Materialia 15 (2021) 101037.

[35] D. Tytko, P.-P. Choi, J. Klöwer, A. Kostka, G. Inden, D. Raabe, Microstructural evolution of a Ni-based superalloy (617B) at 700 °C studied by electron microscopy and atom probe tomography, Acta Mater 60 (2012) 1731–1740.

[36] R.K. Sidhu, O.A. Ojo, M.C. Chaturvedi, Microstructural response of directionally solidified rené 80 superalloy to gas-tungsten arc welding, Metall. Mater. Trans. A 40 (2008) 150–162.

[37] A.T. Egbewande, R.A. Buckson, O.A. Ojo, Analysis of laser beam weldability of Inconel 738 superalloy, Mater. Charact. 61 (2010) 569–574.

[38] M. Zhong, H. Sun, W. Liu, X. Zhu, J. He, Boundary liquation and interface cracking characterization in laser deposition of Inconel 738 on directionally solidified Ni-based superalloy, Scr. Mater. 53 (2005) 159–164.

[39] J.P. Perdew, Y. Wang, Pair-distribution function and its coupling-constant average for the spin-polarized electron gas, Phys. Rev. B 46 (1992) 12947–12954.

[40] J. Wang, M. Enomoto, C. Shang, First-principles study on the interfacial segregation at coherent Cu precipitate/Fe matrix interface, Scr. Mater. 185 (2020) 42–46.

[41] J. Wang, R. Janisch, G.K.H. Madsen, R. Drautz, First-principles study of carbon segregation in bcc iron symmetrical tilt grain boundaries, Acta Mater 115 (2016) 259–268.

[42] T.L. Achmad, W. Fu, H. Chen, C. Zhang, Z.-G. Yang, Effect of solute segregation on the intrinsic stacking fault energy of Co-based binary alloys: a first-principles study, J. Alloy. Compd. 748 (2018) 328–337.

[43] A. Sato, Y.L. Chiu, R.C. Reed, Oxidation of nickel-based single-crystal superalloys for industrial gas turbine applications, Acta Mater 59 (2011) 225–240.

[44] R. Reed, Z. Zhu, A. Sato, D. Crudden, Isolation and testing of new single crystal Superalloys using alloys-by-design method, Mater. Sci. Eng. A 667 (2016) 261–278.

[45] H. Roth, C. Davis, R. Thomson, Modeling solid solution strengthening in nickel alloys, Metall. Mater. Trans. A 28 (1997) 1329–1335.

[46] B. Bocklund, L.D. Bobbio, R.A. Otis, A.M. Beese, Z.-K. Liu, Experimental validation of Scheil–Gulliver simulations for gradient path planning in additively manufactured functionally graded materials, Materialia 11 (2020) 100689.

[47] C.J. Todaro, M. Rashidi, R.L. Liu, S. Gao, T.P. Le, J.E. Fronda, J. Setyadji, Y. T. Tang, M. Seita, Laser powder bed fusion of high-strength and corrosion-resistant Inconel alloy 725, Mater. Charact. 194 (2022) 112454.

[48] Y. Lv, Z. Zhang, Q. Zhang, R. Wang, G. Sun, X. Chen, H. Yu, Z. Bi, J. Xie, G. Wei, Cracking inhibition behavior and the strengthening effect of TiC particles on the CM247LC superalloy prepared by selective laser melting, Mater. Sci. Eng. A 858 (2022) 144119.

[49] B. Guo, Y. Zhang, Z. Yang, D. Cui, F. He, J. Li, Z. Wang, X. Lin, J. Wang, Cracking mechanism of Hastelloy X superalloy during directed energy deposition additive manufacturing, Addit. Manuf. 55 (2022) 102792.

[50] A. Chakraborty, R. Tangestani, W. Muhammad, T. Sabiston, J.-P. Masse, R. Batmaz, A. Wessman, É. Martin, Micro-cracking mechanism of RENÉ 108 thin-wall components built by laser powder bed fusion additive manufacturing, Mater. Today Commun. 30 (2022) 103139.

[51] A. Fardan, U. Klement, H. Brodin, E. Hryha, Effect of part thickness and build angle on the microstructure, surface roughness, and mechanical properties of additively manufactured IN-939, Metall. Mater. Trans. A 54 (2023) 1792–1807.

[52] S.K. Nayak, S.K. Mishra, A.N. Jinoop, C.P. Paul, K.S. Bindra, Experimental studies on laser additive manufacturing of inconel-625 structures using powder bed fusion at 100 μm layer thickness, J. Mater. Eng. Perform. 29 (2020) 7636–7647.

[53] K. Moussaoui, W. Rubio, M. Mousseigne, T. Sultan, F. Rezai, Effects of Selective Laser Melting additive manufacturing parameters of Inconel 718 on porosity, microstructure and mechanical properties, Mater. Sci. Eng. A 735 (2018) 182–190.

[54] N. Lu, Z. Lei, K. Hu, X. Yu, P. Li, J. Bi, S. Wu, Y. Chen, Hot cracking behavior and mechanism of a third-generation Ni-based single-crystal superalloy during directed energy deposition, Addit. Manuf. 34 (2020) 101228.

[55] P. Liu, Z. Wang, Y. Xiao, M.F. Horstemeyer, X. Cui, L. Chen, Insight into the mechanisms of columnar to equiaxed grain transition during metallic additive manufacturing, Addit. Manuf. 26 (2019) 22–29.

[56] A. Prasad, L. Yuan, P. Lee, M. Patel, D. Qiu, M. Easton, D. StJohn, Towards understanding grain nucleation under Additive Manufacturing solidification conditions, Acta Mater 195 (2020) 392–403.

[57] G. Bi, C.-N. Sun, H.-c. Chen, F.L. Ng, C.C.K. Ma, Microstructure and tensile properties of superalloy IN100 fabricated by micro-laser aided additive manufacturing, Mater. Des. 60 (2014) 401–408.

[58] H. Wang, X. Zhang, G.B. Wang, J. Shen, G.Q. Zhang, Y.P. Li, M. Yan, Selective laser melting of the hard-to-weld IN738LC superalloy: efforts to mitigate defects and the resultant microstructural and mechanical properties, J. Alloy. Compd. 807 (2019) 151662.

[59] A. Ramakrishnan, G.P. Dinda, Direct laser metal deposition of Inconel 738, Mater. Sci. Eng. A 740 (2019) 1–13.

[60] J. Xu, X. Lin, P. Guo, Y. Hu, X. Wen, L. Xue, J. Liu, W. Huang, The effect of preheating on microstructure and mechanical properties of laser solid forming IN-738LC alloy, Mater. Sci. Eng. A 691 (2017) 71–80.

[61] J. Li, H.M. Wang, H.B. Tang, Effect of heat treatment on microstructure and mechanical properties of laser melting deposited Ni-base superalloy Rene$'$41, Mater. Sci. Eng. A 550 (2012) 97–102.

[62] J.N. Ghoussoub, P. Klupś, W.J.B. Dick-Cleland, K.E. Rankin, S. Utada, P.A.J. Bagot, D.G. McCartney, Y.T. Tang, R.C. Reed, A new class of alumina-forming superalloy for 3D printing, Addit. Manuf 52 (2022) 102608.

[63] J.N. Ghoussoub, S. Utada, F. Pedraza, W.J.B. Dick-Cleland, Y.T. Tang, R.C. Reed, Alloy design for additive manufacturing: early-stage oxidation of nickel-based Superalloys, Metall. Mater. Trans. A 54 (2022) 1721–1729.